



Article

Research on the Detection Method for Feeding Metallic Foreign Objects in Coal Mine Crushers Based on Reflective Pulsed Eddy Current Testing

Benchang Meng D, Zezheng Zhuang, Jiahao Ma and Sihai Zhao *

School of Mechanical and Electrical Engineering, China University of Mining and Technology–Beijing, Beijing 100083, China; mbc@student.cumtb.edu.cn (B.M.); zhuangzz@student.cumtb.edu.cn (Z.Z.); mjh@student.cumtb.edu.cn (J.M.)

* Correspondence: zsh@cumtb.edu.cn; Tel.: +86-135-0105-7169

Abstract: In response to the difficulties and poor timeliness in detecting feeding metallic foreign objects during high-yield continuous crushing operations in coal mines, this paper proposes a new method for detecting metallic foreign objects, combining pulsed eddy current testing with the Truncated Region Eigenfunction Expansion (TREE) method. This method is suitable for the harsh working conditions in coal mine crushing stations, which include high dust, strong vibration, strong electromagnetic interference, and low temperatures in winter. A model of the eddy current field of feeding metallic foreign objects in the truncated region is established using a coaxial excitation and receiving coil with a Hall sensor. The full-cycle time-domain analytical solution for the induced voltage and magnetic induction intensity of the reflective field under practical square wave signals is obtained. Simulation and experimental results show that the effective time range, peak value, and time to peak of the received voltage and magnetic induction signals can be used to classify and identify the size, thickness, conductivity, and magnetic permeability of feeding metallic foreign objects. Experimental results meet the actual needs for removing feeding metallic foreign objects in coal mine sites. This provides core technical support for the establishment of a predictive fault diagnosis system for crushing equipment.

Keywords: crusher; feeding materials identification; predictive fault diagnosis; pulsed eddy current testing; Truncated Region Eigenfunction Expansion (TREE) method



Citation: Meng, B.; Zhuang, Z.; Ma, J.; Zhao, S. Research on the Detection Method for Feeding Metallic Foreign Objects in Coal Mine Crushers Based on Reflective Pulsed Eddy Current Testing. *Appl. Sci.* 2024, 14, 11704. https://doi.org/10.3390/app 142411704

Received: 9 November 2024 Revised: 4 December 2024 Accepted: 12 December 2024 Published: 15 December 2024



Copyright: © 2024 by the authors. Licensee MDPI, Basel, Switzerland. This article is an open access article distributed under the terms and conditions of the Creative Commons Attribution (CC BY) license (https://creativecommons.org/licenses/by/4.0/).

1. Introduction

Coal, as the most fundamental energy source for industrial production in China, consistently accounts for more than 65% of the total primary energy production. The proportion of open-pit coal mines in the total coal mine production capacity has increased from 2.7% in 1980 to the current 23%. The crushing station, as the core equipment of the semi-continuous process system in open-pit coal mining, is critical, as any failure in this equipment can lead to prolonged idle or downtime in other parts of the system. The early warning of feeding metallic foreign objects in crushers is becoming increasingly important for ensuring the safety and continuous production of coal mines.

The feeding material composition at the crushing station of open-pit coal mines is the most complex, with the largest crushing particle size and the highest difficulty in sensor placement, playing a key role in linking the various stages of the entire semi-continuous production process. The falling of large metallic foreign objects onto the crusher could cause cracks or even fractures at the tips and roots of the crusher's teeth. In particular, large metallic objects exceeding the crusher's discharge particle size could cause the motor to stop and overheat, leading to damage and blocking of the material feeding path between the crusher teeth. In severe cases, a return-to-factory overhaul is required, which is time-

Appl. Sci. 2024, 14, 11704 2 of 17

consuming and costly. Therefore, the classification and identification of feeding metallic foreign objects in crushers is crucial.

Currently, there is no systematic research on the classification and identification of feeding metallic foreign objects in crushers. Bi et al. [1,2] classified and identified feeding coal, iron objects, and wood by collecting the sound and vibration signals of the crusher. However, this detection method has poor timeliness and cannot quantitatively classify and identify the characteristic parameters of feeding metallic foreign objects. Therefore, there is an urgent need to address this issue, and a predictive fault diagnosis method for detecting feeding metallic foreign objects in crushers needs to be proposed.

In large coal mines with an annual production capacity of 35 million tons, the material layer thickness of the plate feeder can reach 0.5 m, and common metallic foreign objects include electric shovel bucket teeth, road grader blades, etc. The high production capacity and continuous operations in coal mines, along with the harsh detection environment under complex working conditions, limit the use of most sensors, such as ultrasonic testing (UT), image recognition sensors, and others. Therefore, this paper proposes a new method for the quantitative detection of feeding metallic foreign objects, combining pulsed eddy current testing and the truncated region eigenfunction function expansion method, tailored to the operating conditions.

Pulsed Eddy Current (PEC) Testing technology is characterized by low cost, fast detection speed, and high sensitivity. With its rich spectral components, it enables noncontact, all-weather detection in harsh environments [3–6]. Currently, many scholars at home and abroad have conducted extensive research on eddy current forward problems and feature classification recognition. There are two methods for acquiring time-domain PEC signals: Fourier transform [7,8] and Laplace transform [9,10]. Theodoulidis and Kriezis [11] used Dirichlet boundary conditions to represent the integral form of the analytical solution in series form. They optimized and extended the Dodd and Deeds model [12]. They innovatively proposed the Truncated Region Eigenfunction Expansion (TREE) method. Li et al. [13,14] employed the Expanded Truncated Region Eigenfunction Expansion (ETREE) method to establish a PEC analytical model for the magnetic field. Tian and Sophian [15] proposed a method using normalization and two reference signals to reduce liftoff problems, applicable for measuring the thickness of metals with various coatings. Skarlatos et al. [16] calculated the transient response of the induced coil above an infinite conductive plate in the time domain by combining a semi-analytical modal expansion method with Euler integration scheme. Theodoulidis et al. [17] proposed a new method called the Sturm-Liouville Global Function (SLGF) for calculating complex eigenvalues in eddy current problems, which can obtain results in a very short time. Huang et al. [18] proposed a new Finite Region Eigenfunction Expansion (FREE) method, which can achieve planar dimension measurement of metallic plates by utilizing peak frequency features.

Wen et al. [19] used the lift-off point of intersection (LOI) in the pulsed eddy current response signal of ferromagnetic test pieces to detect their conductivity, magnetic permeability, and thickness. Xue et al. [20] obtained the log-log method (LLM) by taking the logarithm of power fitting equation, where the linearity and slope can be used to detect metal plates with different conductivities. Ma et al. [21] proposed a high conductivity resolution alloy classification method based on single-frequency eddy current (EC) sensing technology. Qian et al. [22] proposed a Pulse Eddy Current Testing (PECT) method that combines multidimensional features and classification algorithms to identify bearing steel, rebar steel types, and heating defects. Cao et al. [23] innovatively combined Eddy Current Testing (ECT) with deep learning, utilizing the nonlinear fitting ability of neural networks to distinguish between five types of metal materials. Huang et al. [24] introduced the conductivity point of intersection (CPI) feature for noncoaxial T-R sensors in PEC, where the magnitude of the CPI is primarily related to the sensor parameters and sample thickness, and the thickness of the sample and the lift-off of sensor were precisely inverted using the improved Newton–Raphson method.

Appl. Sci. 2024, 14, 11704 3 of 17

The mining truck directly dumps the raw coal material into the ore receiving hopper. A large amount of raw coal material is transported into the crusher through the plate feeder. Due to the vibration of the plate feeder and large density of raw coal material, metallic foreign objects tend to sink to the bottom of the material during transportation. Therefore, in this paper, a rectangular-section coil and Hall sensor array are arranged beneath the outlet of the plate feeder to conduct quantitative detection and analysis of feeding metallic foreign objects, as shown in Figure 1. This study is focused on the SANDVIK dual-roll screening crusher CR610/14-35 (Sandvik Rock Processing Solutions, Stockholm, Sweden), with removable eagle-beak-shaped crusher teeth and a maximum discharge particle size of 300 mm, as shown in Figure 2.

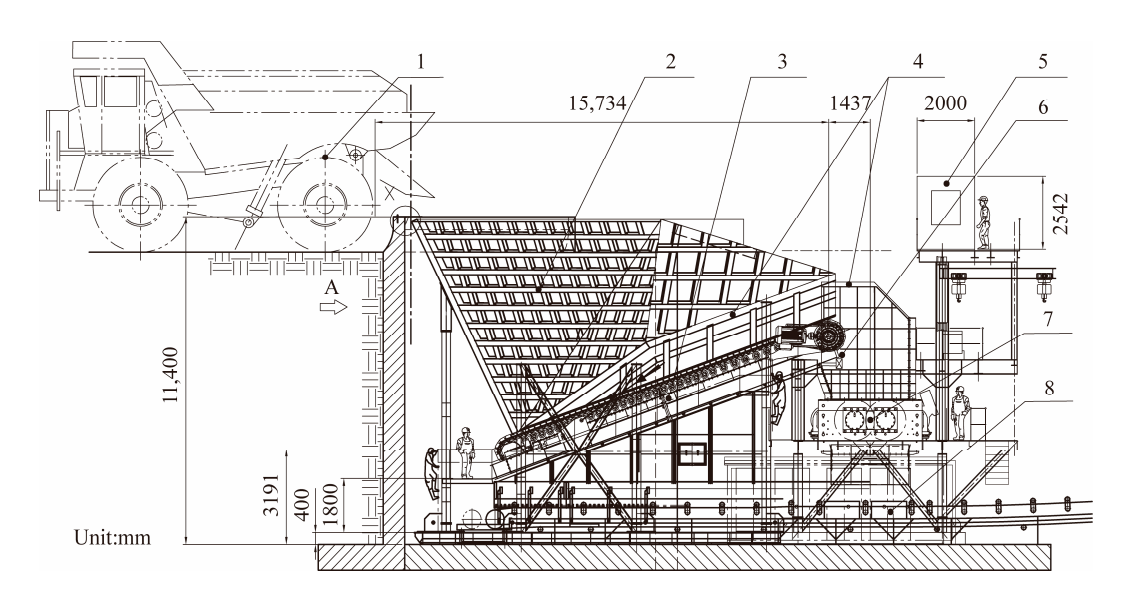


Figure 1. Structure diagram of the open-pit coal mine crushing station (1—Mining Truck, 2—Ore Receiving Hopper, 3—Plate Feeder, 4—Protective Steel Structure, 5—Electrical Control Room, 6—Detection Probes Array, 7—Dual-roll Screening Crusher, and 8—Belt Conveyor).

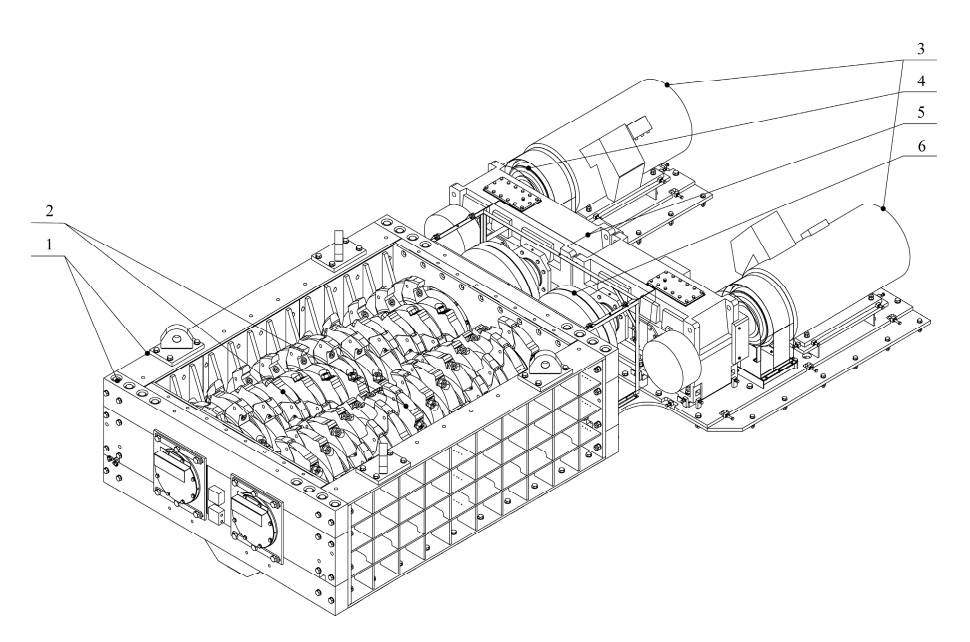


Figure 2. Structure diagram of the dual-roll screening crusher (1—Wear Plates for Front and Side Walls, 2—Crusher Tooth Rolls, 3—Drive Motor, 4—Hydraulic Coupling, 5—Reducer, and 6—Coupling).

To address the complex issues of material type and size of feeding metallic foreign objects, and to improve the robustness of the detection system, a reflective double-coil

Appl. Sci. 2024, 14, 11704 4 of 17

and Hall sensor array was designed to quantitatively classify and identify the characteristics of metallic foreign objects. A theoretical analysis model was established, internal design parameters were optimized, an engineering prototype was fabricated, and on-site experimental verification was conducted.

The rest of this paper is organized as follows: Section 2 presents the frequency domain analytical expressions for the induced voltage and magnetic induction intensity of the metallic foreign object truncated pulsed eddy current field. Section 3 calculates the time-domain expressions for the induced voltage and magnetic induction intensity of the reflective field under actual square wave current signals. Section 4 discusses the results of simulations and experiments, and compares and analyzes the simulation results with the experimental ones. Section 5 summarizes the research work in this paper.

2. System Design and Modeling

According to the introduction in the previous section, the theoretical model for the air layer, metallic foreign object layer, and coal layer is established based on the actual site conditions. Figure 3a shows the side view of the truncated region eddy current field model of the single-turn excitation coil and feeding metallic foreign objects.

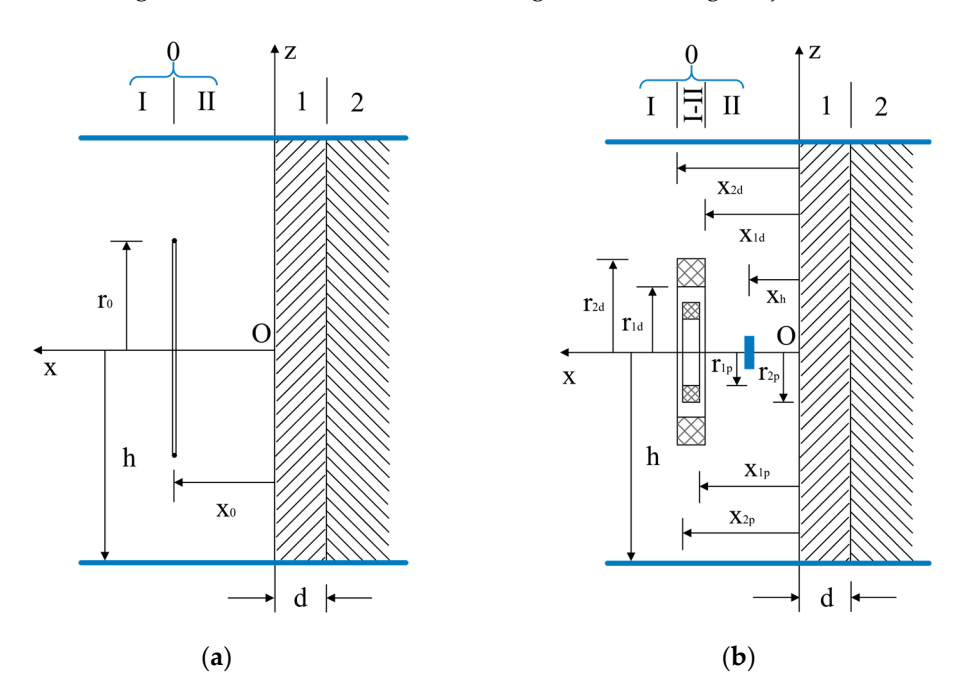


Figure 3. Side view of the truncated region of (a) the single-turn coil, and (b) the rectangular cross-section coaxial excitation and receiving coils with Hall sensors.

First, a cylindrical coordinate system or φx is established, dividing the field into four regions: I, II, 1, and 2. These regions represent the area where the single-turn coil is far from the detection target along the x-axis, the area where the single-turn coil is close to the detection target along the x-axis, the metallic foreign object region, and the feeding coal layer region, respectively. Regions I and II can be combined into region 0. As shown in the diagram, the radius of the single-turn coil is r_0 , the distance between the coil and the metallic foreign object layer is x_0 , the radius of the truncated region is h, and the thickness of the metallic foreign object layer is d.

Next, the magnetic vector potential \hat{A} is taken as the object of solution. Since the cylindrical coil with a rectangular cross-section is axially symmetric about the x-axis, the magnetic vector potential only has an azimuthal component $A_{\varphi}(r,x)$. Based on the Laplace operators for scalars and vectors in cylindrical coordinates [25,26], and using Green's

Appl. Sci. **2024**, 14, 11704 5 of 17

function [27], the expression for the azimuthal component of the magnetic vector potential can be derived from Maxwell's equations:

$$\frac{\partial A_{\varphi}}{\partial r} + \frac{\partial^2 A_{\varphi}}{\partial x^2} - \frac{A_{\varphi}}{r^2} - \mu \sigma \frac{\partial A_{\varphi}}{\partial t} + \mu I \delta(r - r_0) \delta(x - x_0) = 0 \tag{1}$$

where σ is the electrical conductivity. $\mu = \mu_0 \mu_r$, μ is the magnetic permeability, with μ_0 being the permeability of free space and μ_r being the relative magnetic permeability, and I is the amplitude of the excitation current. Then, taking t as the independent variable, the Fourier transform of the azimuthal component of the magnetic vector potential is performed to convert the time domain to the frequency domain, denoted as:

$$\widetilde{A} = \int_{-\infty}^{+\infty} A_{\varphi}(t) e^{-j\omega t} dt$$
 (2)

Taking r as the independent variable, the Hankel transform is performed on $\widetilde{A}(r,x)$ over the interval [0,h], denoted as:

$$\widetilde{A}_{H}(\lambda_{i}, x) = \int_{0}^{h} \widetilde{A}(r, x) r J_{1}(\lambda_{i} r) dr$$
(3)

where λ_i is the *i*-th positive root of $J_1(\lambda_i h) = 0$. Using integration by parts and the general solution of the first-order Bessel function, the expression becomes:

$$-\lambda_i^2 \widetilde{A}_{H}(\lambda_i, \mathbf{x}) + \frac{\partial^2 \widetilde{A}_{H}(\lambda_i, \mathbf{x})}{\partial \mathbf{x}^2} - s^2 \widetilde{A}_{H}(\lambda_i, \mathbf{x}) + \mu \widetilde{I} r_0 \mathbf{J}_1(\lambda_i r_0) \delta(\mathbf{x} - \mathbf{x}_0) = 0$$
 (4)

where in region 0, $s^2 = 0$, and in regions 1 and 2, $s^2 = j\omega\mu\sigma$. According to the general solution of ordinary differential equations, and satisfying the conditions that $C(\lambda_i)$ approaches 0 as $x \to +\infty$ and $D(\lambda_i)$ approaches 0 as $x \to -\infty$, we obtain:

$$\widetilde{A}_{H}(\lambda_{i}, \mathbf{x}) = \sum_{i=1}^{\infty} \left[C(\lambda_{i}) e^{\gamma_{k} \mathbf{x}} + D(\lambda_{i}) e^{-\gamma_{k} \mathbf{x}} \right]$$
(5)

where $\gamma_k = \sqrt{\lambda_i^2 + j\omega\mu_0\mu_{rk}\sigma_k}$ (k = 0, 1, 2). First, consider only the single-turn excitation coil in region 0, ignoring the effects of the receiving coil, Hall sensor, and metallic foreign objects. The boundary conditions at $x = x_0$ for regions I and II can be obtained as:

$$\widetilde{A}_{\mathrm{H}}^{\mathrm{I}}(\lambda_{i}, x_{0}) = \widetilde{A}_{\mathrm{H}}^{\mathrm{II}}(\lambda_{i}, x_{0}) \tag{6}$$

$$\frac{\partial \widetilde{A}_{H}^{I}}{\partial x}\bigg|_{x=r_{0}} = \frac{\partial \widetilde{A}_{H}^{II}}{\partial x}\bigg|_{x=r_{0}} - \mu_{0}\widetilde{I}r_{0}J_{1}(\lambda_{i}r_{0})$$
 (7)

Solving the equation, the excitation field coefficient is obtained as:

$$C_S = C_{\rm II} = \frac{\mu_0 \widetilde{I}}{2\lambda_i} r_0 J_1(\lambda_i r_0) e^{-\lambda_i x_0}$$
(8)

Next, merging regions I and II into region 0, and adding the effect of the metallic medium, the boundary conditions at the interface $x = x_k$ (k = 1, 2) between regions k - 1 and k can be obtained as:

$$\widetilde{A}_{Hk-1}(\lambda_i, \mathbf{x}_k) = \widetilde{A}_{Hk}(\lambda_i, \mathbf{x}_k) \tag{9}$$

$$\frac{1}{\mu_{rk-1}} \frac{\partial \widetilde{A}_{Hk-1}}{\partial x} \bigg|_{x=x_k} = \frac{1}{\mu_{rk}} \frac{\partial \widetilde{A}_{Hk}}{\partial x} \bigg|_{x=x_k}$$
(10)

Appl. Sci. 2024, 14, 11704 6 of 17

Solving the equation, the reflection field coefficient is obtained as:

$$D_{ref} = D_0 = \frac{\mu_0 \widetilde{I}}{2\lambda_i} r_0 \widetilde{R} J_1(\lambda_i r_0) e^{-\lambda_i x_0}$$
(11)

where $\widetilde{R} = \frac{e^{2\gamma_1 d}(\gamma_1 \mu_{r2} + \gamma_2 \mu_{r1})(\lambda_i \mu_{r1} - \gamma_1) + (\gamma_1 \mu_{r2} - \gamma_2 \mu_{r1})(\lambda_i \mu_{r1} + \gamma_1)}{e^{2\gamma_1 d}(\gamma_1 \mu_{r2} + \gamma_2 \mu_{r1})(\lambda_i \mu_{r1} + \gamma_1) + (\gamma_1 \mu_{r2} - \gamma_2 \mu_{r1})(\lambda_i \mu_{r1} - \gamma_1)}$. Thus, we obtain $\widetilde{A}_{HS}(\lambda_i, x) = \sum_{i=1}^{\infty} C_S e^{\lambda_i x}$, $\widetilde{A}_{Href}(\lambda_i, x) = \sum_{i=1}^{\infty} D_{ref} e^{-\lambda_i x}$. Taking λ_i as the independent variable, the inverse

Hankel transform is performed on $\widetilde{A}_{HS}(\lambda_i,x)$ and $\widetilde{A}_{Href}(\lambda_i,x)$ over the interval [0, h], yielding:

$$\widetilde{A}_S(r, x, r_0, x_0) = \sum_{i=1}^{\infty} \frac{\mu_0 \widetilde{I} J_1(\lambda_i r)}{\lambda_i h^2 J_0^2(\lambda_i h)} r_0 J_1(\lambda_i r_0) e^{\lambda_i (x - x_0)}$$
(12)

$$\widetilde{A}_{ref}(r, x, r_0, x_0) = \sum_{i=1}^{\infty} \frac{\mu_0 \widetilde{I} J_1(\lambda_i r)}{\lambda_i h^2 J_0^2(\lambda_i h)} r_0 \widetilde{R} J_1(\lambda_i r_0) e^{-\lambda_i (x + x_0)}$$
(13)

Next, by considering the rectangular cross-section coaxial excitation and receiving coils with Hall sensors, we establish the truncated region eddy current field model as shown in Figure 3b. The current I in the single-turn excitation coil is replaced with the current density in the excitation coil's rectangular cross-section, denoted as i_0 , satisfying the condition $\tilde{i}_0 = N_1 \tilde{I} / (r_{2d} - r_{1d})(x_{2d} - x_{1d})$.

Since the radial dimension of the Hall sensor is small, its magnetic induction intensity in the z-axis direction can be neglected, and only its magnetic induction intensity in the x-axis direction is considered. The formula for the magnetic induction intensity of the Hall sensor and the induced voltage formula for the receiving coil can be derived and are denoted as:

$$\widetilde{B} = \widetilde{B}_{air} + \widetilde{B}_{ref} = \int_{x_{1d}}^{x_{2d}} \int_{r_{1d}}^{r_{2d}} \frac{1}{r} \frac{\partial \left\{ r \left[\widetilde{A}_S(r, x, r_0, x_0) + \widetilde{A}_{ref}(r, x, r_0, x_0) \right] \right\}}{\partial r} dr_0 dx_0$$
 (14)

$$\widetilde{U} = \widetilde{U}_{air} + \widetilde{U}_{ref} = \int_{x_{1p}}^{x_{2p}} \int_{r_{1p}}^{r_{2p}} \frac{j\omega 2\pi r N_2}{\left(r_{2p} - r_{1p}\right)\left(x_{2p} - x_{1p}\right)} \left\{ \int_{x_{1d}}^{x_{2d}} \int_{r_{1d}}^{r_{2d}} \left[\widetilde{A}_S(r, x, r_0, x_0) + \widetilde{A}_{ref}(r, x, r_0, x_0) \right] dr_0 dx_0 \right\} dr dx \quad (15)$$

Substituting Equations (12) and (13) into Equations (14) and (15), and using the recurrence relation of the Bessel function, along with the definition of the double integral, and replacing the Fourier variable $j\omega$ with the Laplace variable p, we obtain:

$$B(p) = \sum_{i=1}^{\infty} \frac{\mu_0 I(p) Y(\lambda_i)}{h^2 J_0^2(\lambda_i h)} \left[e^{\lambda_i x_h} + R(p) e^{-\lambda_i x_h} \right]$$
 (16)

$$U(p) = 2\pi\mu_0 \sum_{i=1}^{\infty} \frac{pI(p)Y(\lambda_i)}{\lambda_i h^2 J_0^2(\lambda_i h)} \Big[Y_S(\lambda_i) + R(p)Y_{ref}(\lambda_i) \Big]$$
(17)

In Equations (16) and (17)

$$Y(\lambda_i) = \frac{N_1 \left[r_{2d}^2 \chi(\lambda_i r_{2d}) - r_{1d}^2 \chi(\lambda_i r_{1d}) \right] \left(e^{-\lambda_i x_{2d}} - e^{-\lambda_i x_{1d}} \right)}{-\lambda_i (r_{2d} - r_{1d}) (x_{2d} - x_{1d})}$$
(18)

$$Y_{S}(\lambda_{i}) = \frac{N_{2} \left[r_{2p}^{2} \chi(\lambda_{i} r_{2p}) - r_{1p}^{2} \chi(\lambda_{i} r_{1p}) \right] \left(e^{\lambda_{i} x_{2p}} - e^{\lambda_{i} x_{1p}} \right)}{\lambda_{i} (r_{2p} - r_{1p}) \left(x_{2p} - x_{1p} \right)}$$
(19)

$$Y_{ref}(\lambda_i) = \frac{N_2 \left[r_{2p}^2 \chi(\lambda_i r_{2p}) - r_{1p}^2 \chi(\lambda_i r_{1p}) \right] \left(e^{-\lambda_i x_{2p}} - e^{-\lambda_i x_{1p}} \right)}{-\lambda_i \left(r_{2p} - r_{1p} \right) \left(x_{2p} - x_{1p} \right)}$$
(20)

$$\chi(\lambda_i) = \int_0^1 J_1(\lambda_i r_0) r_0 dr_0 = \frac{\pi}{2\lambda_i} [J_1(\lambda_i) \mathbf{H}_0(\lambda_i) - J_0(\lambda_i) \mathbf{H}_1(\lambda_i)]$$
 (21)

$$R(p) = \frac{e^{2\gamma_1'd}(\gamma_1'\mu_{r2} + \gamma_2'\mu_{r1})(\lambda_i\mu_{r1} - \gamma_1') + (\gamma_1'\mu_{r2} - \gamma_2'\mu_{r1})(\lambda_i\mu_{r1} + \gamma_1')}{e^{2\gamma_1'd}(\gamma_1'\mu_{r2} + \gamma_2'\mu_{r1})(\lambda_i\mu_{r1} + \gamma_1') + (\gamma_1'\mu_{r2} - \gamma_2'\mu_{r1})(\lambda_i\mu_{r1} - \gamma_1')}$$
(22)

$$\gamma_k' = \sqrt{\lambda_i^2 + p\mu_0\mu_{rk}\sigma_k} \ (k = 0, 1, 2).$$
 (23)

3. Time-Domain Analytical Solution of the Received Signal

Next, the signal generator applies a square wave voltage signal to the excitation coil. We perform a time-domain analysis of the output voltage signal from the receiving coil and the magnetic induction intensity signal generated by the actual square wave current signal.

3.1. Time-Domain Analytical Solution of the Received Voltage Signal

First, an ideal step current signal is applied to the excitation coil, denoted as:

$$I(p) = I\frac{1}{p} \tag{24}$$

The relative magnetic permeability of coal is 1, and its electrical conductivity is close to 0. Substituting the conditions $\mu_{r1} = \mu_r$, $\sigma_1 = \sigma$, $\mu_{r2} = 1$, and $\sigma_2 = 0$ into Equation (22), the reflection coefficient is obtained as:

$$\Gamma_{U}(p) = pI(p)R(p) = \frac{2I - \frac{2\xi I}{\lambda_{i}\mu_{r}d}(\tan\xi - \cot\xi)}{\left(\tan\xi + \frac{2\xi}{\lambda_{i}\mu_{r}d}\right)\left(\cot\xi - \frac{2\xi}{\lambda_{i}\mu_{r}d}\right)}$$
(25)

where $\xi = -jd\gamma_k'/2$. Thus, we can obtain the relationship between the poles of the equation and the corresponding Laplace variables, yielding:

$$p_{t,c} = -\frac{\lambda_i^2 + (2\xi_{t,c}/d)^2}{\mu_0 \mu_r \sigma}$$
 (26)

According to the Cauchy residue theorem [28], and using the residue calculation property of the poles, we can obtain the inverse Laplace transform of the reflection coefficient, denoted as:

$$f(t) = \frac{1}{2\pi i} \int_0^{+\infty} F(p) e^{pt} dp = \sum_{k=1}^n \text{Res}[F(p) e^{pt}] \bigg|_{p = p_{tk,ck}}$$
(27)

By applying Equation (27) to Equation (25) and substituting the result into Equation (17), we obtain:

$$U_{ref}(t) = \frac{8\pi I}{\sigma d} \sum_{i=1}^{\infty} \frac{Y(\lambda_i) Y_{ref}(\lambda_i)}{h^2 J_0^2(\lambda_i h)} \left[\sum_{k=1}^n \left(A_{tk} e^{p_{tk}t} + A_{ck} e^{p_{ck}t} \right) \right]$$
(28)

where $A_{tk} = -\frac{\xi_{tk}\sin 2\xi_{tk}}{2\cos^2\xi_{tk} + \lambda_i\mu_r d}$, $A_{ck} = \frac{\xi_{ck}\sin 2\xi_{ck}}{2\sin^2\xi_{ck} + \lambda_i\mu_r d}$. ξ_{tk} and ξ_{ck} are the k-th positive poles of equations $\tan \xi = -\frac{2\xi}{\lambda_i\mu_r d}$ and $\cot \xi = \frac{2\xi}{\lambda_i\mu_r d}$, respectively. Finally, we consider the actual rectangular pulse current signal applied to the excitation

Finally, we consider the actual rectangular pulse current signal applied to the excitation coil, $i(t) = I\left[\left(1 - e^{-\frac{t}{\tau_0}}\right)\varepsilon(t) + \left(e^{-\frac{t-\tau}{\tau_0}} - 1\right)\varepsilon(t-\tau)\right](0 \le t \le T)$. Where τ is the pulse width, and τ_0 is the actual rise or fall time of the rise or fall edge. According to the

Appl. Sci. 2024, 14, 11704 8 of 17

convolution theorem, the time-domain expression for the reflected field induced voltage in the receiving coil under actual conditions can be obtained as:

$$U_{ref}(t) = i(t) * \frac{8\pi I}{\sigma d} \sum_{i=1}^{\infty} \frac{Y(\lambda_i) Y_{ref}(\lambda_i)}{h^2 J_0^2(\lambda_i h)} \left[\sum_{k=1}^{n} (A_{tk} e^{p_{tk} t} + A_{ck} e^{p_{ck} t}) \right]$$
(29)

3.2. *Time-Domain Analytical Solution of the Received Magnetic Induction Intensity Signal* 3.2.1. Full-Period Time-Domain Analytical Solution

First, we decompose Equation (22) into $R_0(p) + \sum_{m=1}^{\infty} R_m(p)$. According to the frequency shift and scale transformation properties of the Laplace transform [29], and using the standard Laplace inverse transform formula [30], we can obtain:

$$R_0(t) = \sqrt{\frac{4\mu_r^2 \lambda_i^2}{\pi \tau t}} e^{-\frac{\lambda_i^2 t}{\tau}} - \frac{2\mu_r^2 \lambda_i^2}{\tau} \operatorname{erfc}\left(\mu_r \sqrt{\frac{\lambda_i^2 t}{\tau}}\right) - \delta(t)$$
 (30)

$$R_{m}(t) = \frac{\lambda_{i}^{2} e^{-\lambda_{i}^{2} t/\tau}}{\tau} \left[\sum_{j=0}^{2m} C_{2m}^{j} (-2)^{j+2} \mu_{r}^{j+1} \varphi_{j-1} \left(\mu_{r}, 2m \lambda_{i} d, \frac{\lambda_{i}^{2} t}{\tau} \right) + \sum_{j=0}^{2m-1} C_{2m-1}^{j} (-2)^{j+2} \mu_{r}^{j+3} \varphi_{j+1} \left(\mu_{r}, 2m \lambda_{i} d, \frac{\lambda_{i}^{2} t}{\tau} \right) \right]$$
(31)

where $\tau = \mu_0 \mu_r \sigma$, $\varphi_j(a,k,t) = (4t)^{\frac{j}{2}} e^{ak+a^2t} i^j \operatorname{erfc}\left(a\sqrt{t} + \frac{k}{2\sqrt{t}}\right)$. Erf(x) and erfc(x) represent the error function and complementary error function, respectively, and $i^j \operatorname{erfc}(x)$ is the j-th integral of the complementary error function.

To obtain the time-domain expression for the reflected magnetic induction intensity of the Hall sensor under actual conditions, we first use MATLAB 2023b to perform the fast Fourier transform (FFT) on i(t) and $R_0(t) + \sum\limits_{m=1}^{\infty} R_m(t)$, respectively. After multiplying the two results, we apply the inverse FFT (IFFT) to the product. Finally, the inverse transform result is combined with the remaining part through series operations.

$$B_{ref}(t) = \sum_{i=1}^{\infty} \frac{\mu_0 e^{-\lambda_i x_h} Y(\lambda_i)}{h^2 J_0^2(\lambda_i h)} \cdot \frac{1}{2\pi} \int_{-\infty}^{+\infty} \left[R_0(\omega) + \sum_{m=1}^{\infty} R_m(\omega) \right] \cdot I(\omega) e^{j\omega t} d\omega \tag{32}$$

3.2.2. Time-Domain Analytical Solution for the Rising Half-Cycle

Next, we consider the analysis of the rising edge of the actual square wave current signal applied to the excitation coil. By verifying the above method, the reflection coefficient is obtained as:

$$\Gamma_{B}(p) = I(p)R(p) = \Gamma_{BL0}(p) + \Gamma_{BR0}(p) - \sum_{m=1}^{\infty} \left[\Gamma_{BLm}(p) + \Gamma_{BRm}(p)\right]$$

$$= \left(\frac{I}{p} - \frac{\tau_{0}I}{p\tau_{0} + 1}\right) \left[\frac{\mu_{r}\lambda_{i} + \gamma'}{\mu_{r}\lambda_{i} - \gamma'} - \frac{4\mu_{r}\lambda_{i}\gamma'}{\mu_{r}^{2}\lambda_{i}^{2} - \gamma'^{2}} \sum_{m=0}^{\infty} \left(\frac{\mu_{r}\lambda_{i} - \gamma'}{\mu_{r}\lambda_{i} + \gamma'} \cdot e^{-\gamma'd}\right)^{2m}\right]$$
(33)

By dividing $\Gamma_B(p)$ into terms $\Gamma_{BL0}(p)$ and $\Gamma_{BLm}(p)$ with $\frac{I}{p}$, and terms $\Gamma_{BR0}(p)$ and $\Gamma_{BRm}(p)$ with $\frac{\tau_0 I}{p\tau_0+1}$, the inverse Laplace transform is applied to each separately. For the former, $\frac{I}{p}$ is transformed into $\frac{I\tau}{2\lambda_i}\left[\frac{1}{\sqrt{p\tau+\lambda_i^2}-\lambda_i}-\frac{1}{\sqrt{p\tau+\lambda_i^2}+\lambda_i}\right]$. For the latter, $\frac{\tau_0 I}{p\tau_0+1}$ is transformed into $\frac{I}{2}\sqrt{\frac{\tau}{\nu}}\left[\frac{1}{\sqrt{p\tau+\lambda_i^2}-\sqrt{\tau\nu}}-\frac{1}{\sqrt{p\tau+\lambda_i^2}+\sqrt{\tau\nu}}\right]$, where $\nu=\frac{\lambda_i^2}{\tau}-\frac{1}{\tau_0}$. At this point, the Laplace inverse transform formula can be applied to continue the solution, denoted as:

Appl. Sci. **2024**, 14, 11704 9 of 17

$$\phi_n(a, b, k, t) = \frac{1}{2\pi i} \int_0^{+\infty} \frac{e^{-k\sqrt{p}}}{\sqrt{p}(\sqrt{p} + a)^n (\sqrt{p} + b)} e^{pt} dp$$
 (34)

where $\phi_n(a,b,k,t) = \frac{1}{(a-b)^n} \left[\varphi_0(b,k,t) - \sum_{j=0}^{n-1} (b-a)^j \varphi_j(a,k,t) \right]$. $\Gamma_{BL0}(p)$ and $\Gamma_{BLm}(p)$ are

obtained by using the frequency shift and scale transformation properties of the Laplace transform [29], combined with the standard Laplace inverse transform formula [25], the Laplace inverse transform form can be obtained as:

$$\Gamma_{BL0}(t) = 2\sqrt{\frac{\lambda_i^2 t}{\pi \tau}} e^{-\lambda_i^2 t/\tau} - \left(1 + \frac{2\lambda_i^2 t}{\tau}\right) \operatorname{erfc}\left(\sqrt{\frac{\lambda_i^2 t}{\tau}}\right) + 1 - \varepsilon(t)$$
(35)

$$\Gamma_{BLm}(t) = \Psi\left(\mu_r, 1, 2m\lambda_i d, \frac{\lambda_i^2 t}{\tau}\right) + \left[\sum_{n=1}^{2m} C_{2m}^n (-2)^{n+2} \eta_n \left(\mu_r, 2m\lambda_i d, \frac{\lambda_i^2 t}{\tau}\right) + \sum_{n=0}^{2m-1} C_{2m-1}^n (-2)^{n+2} \eta_{n+2} \left(\mu_r, 2m\lambda_i d, \frac{\lambda_i^2 t}{\tau}\right)\right]$$
(36)

where $\eta_n(a,k,t) = \frac{a^n e^{-t}}{2} [\phi_n(a,-a,k,t) - \phi_n(a,k,t)]$. $\Gamma_{BR0}(p)$ and $\Gamma_{BRm}(p)$ are obtained by using the integral formula of the complementary error function [30], combined with the standard Laplace inverse transform formula [30], the Laplace inverse transform form can be obtained as:

$$\Gamma_{BR0}(t) = \frac{2I\mu_r^2\lambda_i^2}{\mu_r^2\lambda_i^2 - \nu\tau} \left\{ e^{-t/\tau_0} \left[1 - \frac{\sqrt{\nu\tau}}{\mu_r\lambda_i} \operatorname{erf}\sqrt{\nu t} \right] \right. \\ \left. - e^{(\mu_r^2 - 1)\lambda_i^2 t/\tau} \operatorname{erfc}\left(\mu_r\lambda_i\sqrt{\frac{t}{\tau}}\right) \right\} - Ie^{-t/\tau_0}$$
(37)

$$\Gamma_{BRm}(t) = \Psi\left(\mu_r, \frac{\sqrt{\tau\nu}}{\lambda_i}, 2m\lambda_i d, \frac{\lambda_i^2 t}{\tau}\right) + \sum_{n=1}^{2m} C_{2m}^n (-2)^{n+2} \Phi_n\left(\mu_r, \frac{\sqrt{\tau\nu}}{\lambda_i}, 2m\lambda_i d, \frac{\lambda_i^2 t}{\tau}\right) + \sum_{n=0}^{2m-1} C_{2m-1}^n (-2)^{n+2} \Phi_{n+2}\left(\mu_r, \frac{\sqrt{\tau\nu}}{\lambda_i}, 2m\lambda_i d, \frac{\lambda_i^2 t}{\tau}\right)$$
(38)

where $\Psi(a,b,k,t) = \frac{2ae^{-t}I}{b}[\varphi_0(-b,k,t) - \varphi_0(b,k,t)]$, $\Phi_n(a,b,k,t) = \frac{a^{n+1}e^{-t}I}{2b}[\varphi_n(a,-b,k,t) - \varphi_n(a,b,k,t)]$. By substituting Equations (35)–(38) into Equation (16), the following formula can be obtained. It has been verified that this equation achieves the same result as the Section 3.2.1.

$$B_{ref}(t) = \sum_{i=1}^{\infty} \frac{\mu_0 e^{-\lambda_i x_h} Y(\lambda_i)}{h^2 J_0^2(\lambda_i h)} \cdot \Gamma_B(t)$$
(39)

4. Theoretical Simulation and Experimental Verification

4.1. Theoretical Simulation

By subtracting the output signals U(t), B(t) with the metal plate from the output signals Uair(t), Bair(t) without the metal plate, the differential signals Uref(t) and Bref(t) can be obtained. As seen in Figures 4 and 5, the characteristics of ferromagnetic metals are distinctly different from those of non-ferromagnetic metals. For ferromagnetic metals, Uref(t) and Bref(t) are on the same side as U(t) and Uair(t), and Uair(t), and Uair(t), respectively, whereas for non-ferromagnetic metals, they are on opposite sides. This is because under the action of the single probe, ferromagnetic metals are magnetized in the region and cause the output signal U(t) and U(t) and

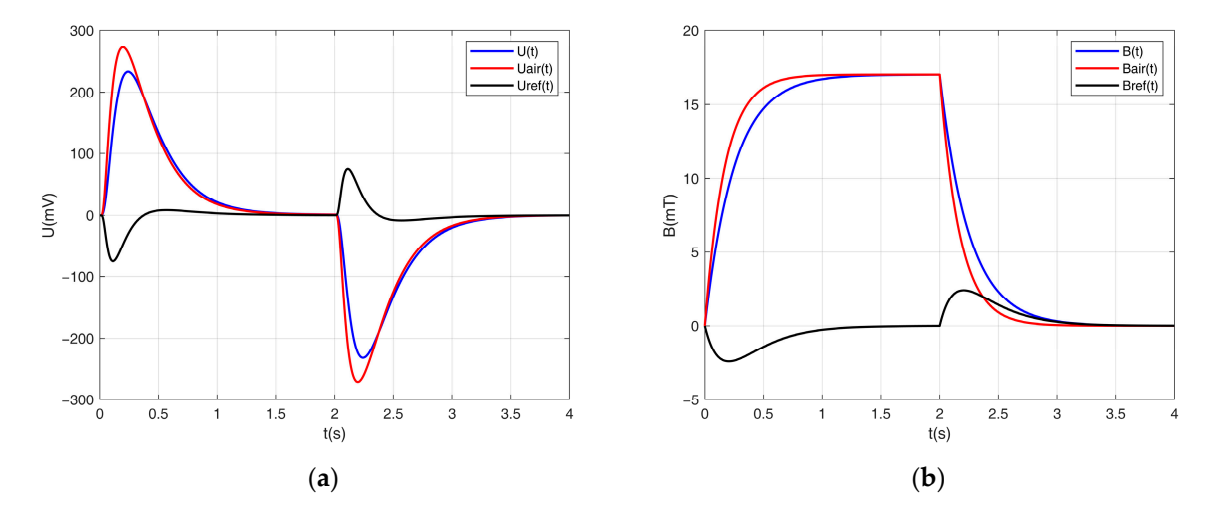


Figure 4. Typical PEC signals with non-ferromagnetic metals; (a) receiving coil voltage signals; (b) magnetic induction signals of Hall sensor.

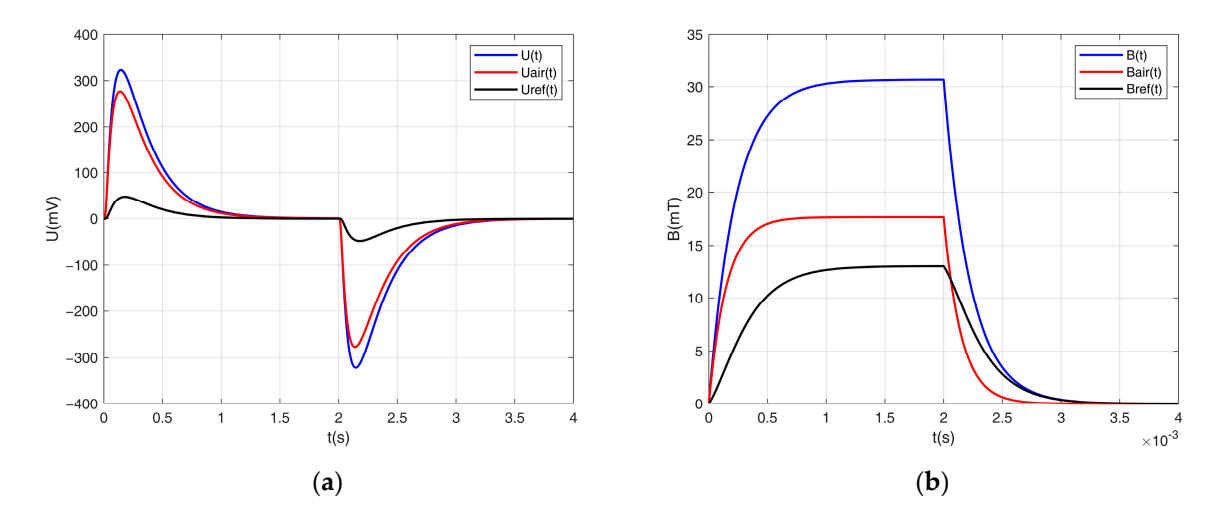


Figure 5. Typical PEC signals with ferromagnetic metals; (a) receiving coil voltage signals; (b) magnetic induction signals of Hall sensor.

4.2. Single-Probe Testing Experiment

In order to better observe the interaction between the rectangular cross-section coaxial excitation, receiving coil, Hall sensor, and the moving metal foreign object, a single-probe testing experimental platform is built, as shown in Figure 6. The signal generator, with a power amplifier, outputs a high-level square wave signal with a 12 V amplitude and a 50% duty cycle. The square wave signal is applied to the excitation coil of the single probe, and the output signals from the receiving coil and Hall sensor are sent through a signal conditioning module to the data acquisition card. The signal conditioning module is a second-order low-pass filter circuit, characterized by fast attenuation and strong filtering effects. The data acquisition card used is Smacq USB-4650 (Smacq Technologies Co., Ltd., Beijing, China), a high-speed acquisition card that transmits data via USB. It has 8 synchronized analog input channels with a sampling rate of 500 kSa/s, a resolution of 16 bits, and an input voltage amplitude of ± 10 V. It is equipped with a DAQUS 2.0 driver and can be programmed using LabVIEW 2021 or MATLAB 2023b software. The PC and data acquisition card are connected via USB. The system block diagram is shown below.

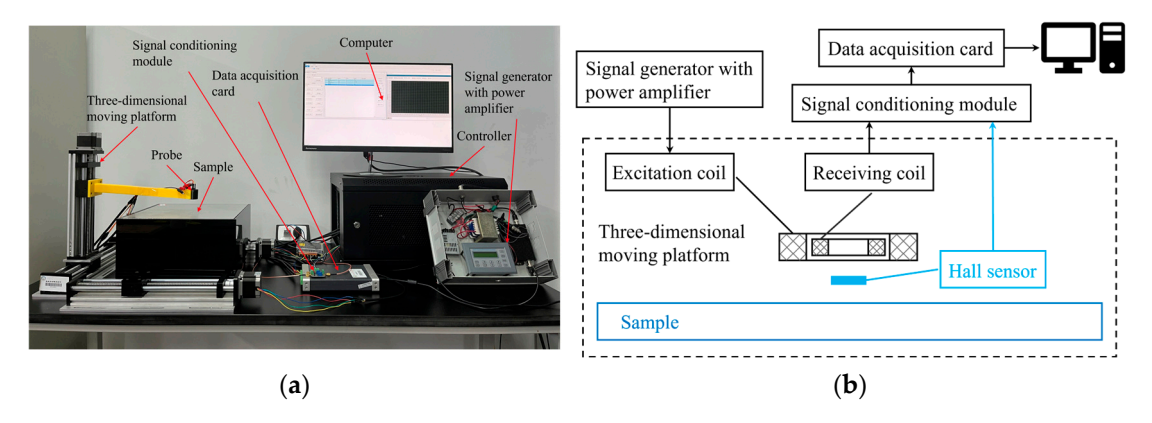


Figure 6. Single-probe testing experiment; (a) experimental platform; (b) block diagram of the system.

The PC is connected to the controller to manipulate the three-dimensional moving platform. The three-dimensional moving platform is responsible for the horizontal and vertical positioning of the single probe and the uniform movement of the metal foreign object. The single-probe coil is a cylindrical hollow coil precisely wound with copper wire, and the Hall sensor is placed at the center of the single probe, as shown in Figure 7a. The Hall sensor selected is a proportional linear Hall effect magnetic sensor with a high-speed detection bandwidth of 20 kHz, a magnetic sensitivity of 51.5 mV/mT, and a range of ± 42 mT. In the experiment, the sensitivity of the coil and Hall sensor is affected by temperature [31]. The resistance of the copper hollow coil is proportional to temperature. As the temperature of the Hall sensor rises from -40 °C to 120 °C, its magnetic sensitivity increases from 46 mV/mT to 56 mV/mT. Therefore, data collection should only be performed after the temperature of the single-probe coil has stabilized. The parameters of the coil used in the experiment are shown in Table 1.

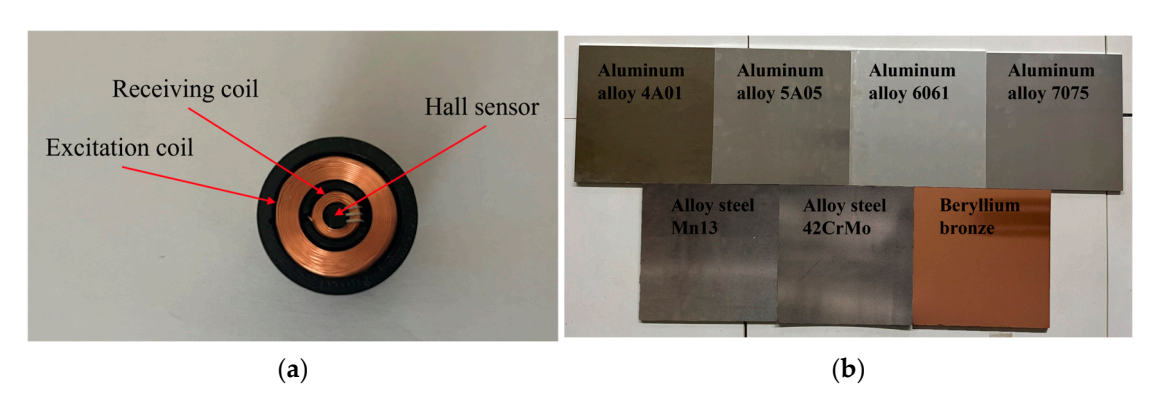


Figure 7. Detailed view of single-probe and samples; (a) bottom view of the single-probe; (b) seven test samples for experiment.

Table 1. Single-probe parameters.

Receiving Coil	Excitation Coil
2.6	7.0
5.0	12.0
3.2	7.1
100	745
5	5
0.06	9.1
-	250
	2.6 5.0 3.2 100 5

The sample dimensions are determined based on the maximum discharge particle size of the SANDVIK dual-roll screening crusher CR610/14-35, which is 300 mm. The length

and width are $300~\text{mm} \times 300~\text{mm}$, with thicknesses chosen as 3~mm, 5~mm, 7~mm, 10~mm, and 12~mm. The materials of the samples are selected from common metal foreign objects found in coal mine crushers, such as alloy steel Mn13, 42CrMo, copper alloy beryllium bronze, aluminum alloys 4A01, 5A05, 6061, and 7075, as shown in Figure 7b. The relative magnetic permeability of the ferromagnetic alloy steel 42CrMo is taken as 60, while the relative magnetic permeability of other metals is 1. The electrical conductivity of the samples is measured using the Autosigma3000 from General Electric Company (Boston, MA, USA), and the conductivity parameters are shown in Table 2.

Table 2. Conductivity of common metal foreign objects in coal mines.

Material Name	Mn13	42CrMo	Beryllium Bronze	4A01	5A05	6061	7075
Conductivity (MS/m)	3.69	6.49	12.76	18.02	20.12	23.26	25.34

Figure 8 above shows the output signal curves of the ferromagnetic alloy steel 42CrMo at five different thicknesses, with the probe lift height set to 5 mm. Figure 9 extracts the relationship between the key characteristic quantities and the thicknesses from Figure 8. The results indicate that as the sample thickness increases, the peak value gradually decreases, while the peak time gradually increases. The differential output signals Uref(t) and Bref(t) from the receiving coil and Hall sensor exhibit the same characteristics. The two results corroborate each other, allowing for more accurate classification and identification of ferromagnetic metals. The simulation used a CPU E-2276M (Intel Corporation, Santa Clara, CA, USA) and MATLAB 2023b, and the simulated data closely matched the measured results.

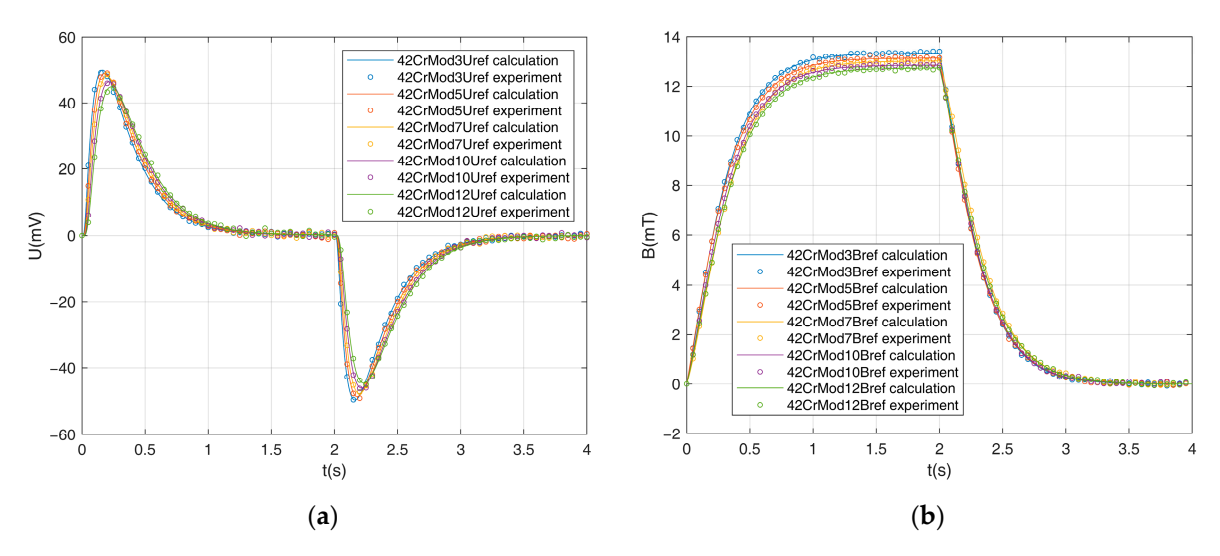


Figure 8. PEC differential signals of alloy steel 42CrMo with different thicknesses; (a) receiving coil differential voltage signals; (b) magnetic induction differential signals of Hall sensor.

Figures 10 and 11 above shows the relationship between key characteristics of pulsed eddy current differential signals and the conductivity and thickness of non-ferromagnetic metals. The results differ from those of ferromagnetic metals. It can be seen that, for non-ferromagnetic metals of the same thickness, as the conductivity increases, both the peak value and peak time also increase. When the conductivity of non-ferromagnetic metals is the same, increasing the thickness leads to higher peak values and longer peak times. However, the effect of conductivity on these two features is more significant than the effect of thickness, whether considering the peak value or the time to peak. This allows for more effective extraction of the conductivity and thickness characteristics of non-ferromagnetic metals.

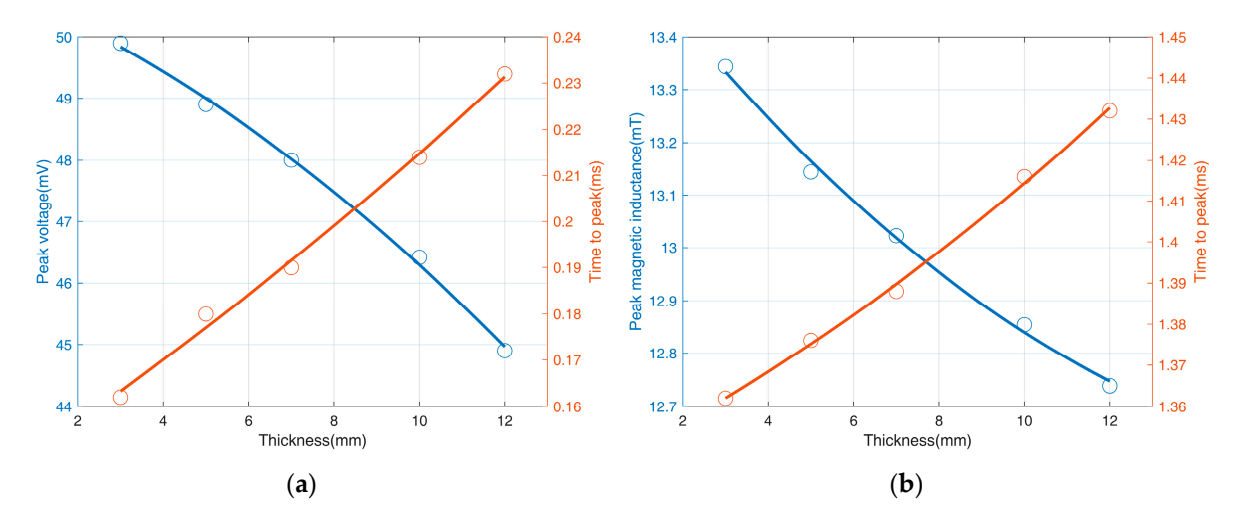


Figure 9. Relationship between key characteristic quantities of PEC differential signals and the thicknesses of alloy steel 42CrMo; (a) peak voltage and its corresponding time to peak; (b) peak magnetic inductance and its corresponding time to peak.

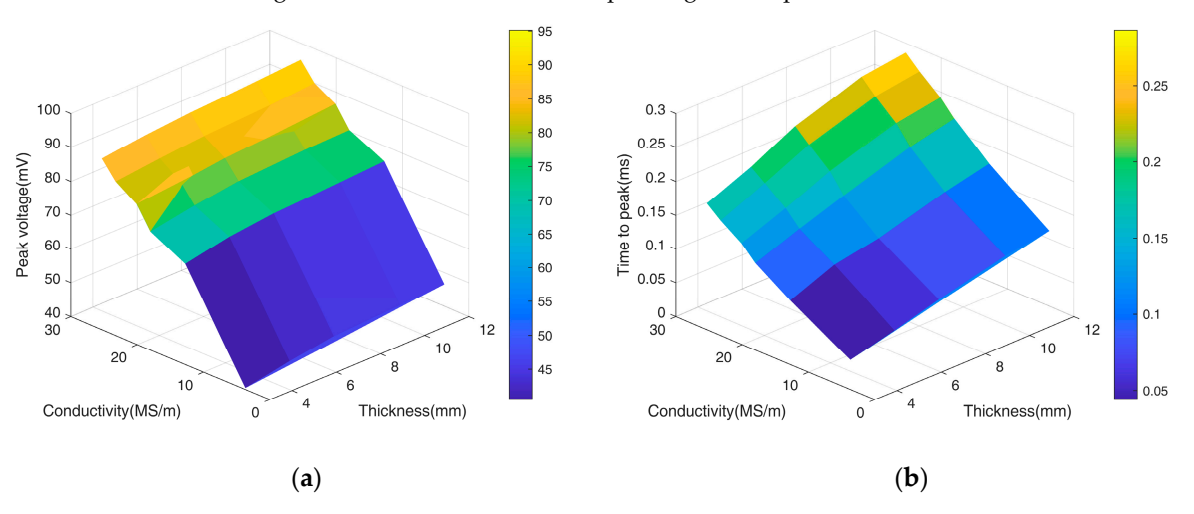


Figure 10. Three-dimensional surface plots between key characteristics of pulsed eddy current differential voltage signals and the conductivity and thickness of non-ferromagnetic metals; (a) peak voltage; (b) time to peak.

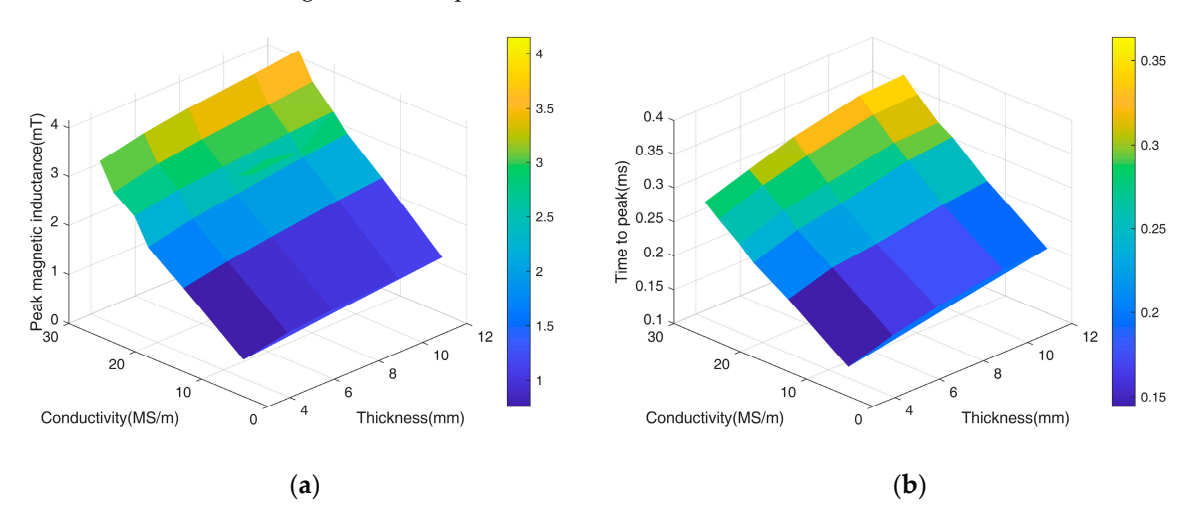


Figure 11. Three-dimensional surface plots between key characteristics of pulsed eddy current differential magnetic inductance signals and the conductivity and thickness of non-ferromagnetic metals; (a) peak magnetic inductance; (b) time to peak.

Appl. Sci. 2024, 14, 11704 14 of 17

4.3. Multi-Probe Array Field Experiment

Figure 12 shows the experimental platform set up to simulate the coal mine site. The belt width of the belt conveyor is 400 mm, and the belt running speed is the same as that at the coal mine site, which is 0.3 m/s. Four multi-probe arrays are set one meter below the exit of the belt conveyor. These four multi-probe arrays are evenly spaced, with a detection range of 300 mm. Data are collected at a horizontal distance of 5 mm from the falling metallic foreign object. The position and horizontal width of the metallic foreign object are determined based on the range of signals received by the multi-probe array. The vertical width of the metallic foreign object is then calculated by the time range of the effective detection signals from the multi-probe array.



Figure 12. Field experiment platform with the multi-probe array.

A 300 \times 300 \times 10 mm alloy steel Mn13 metal plate was selected for the drop test experiment. The signal generator with a power amplifier emitted the same signal as in the single-probe test experiment. After the probe coil temperature stabilized, the experiment was started. The data acquisition card began collecting data when the metal foreign object was about to leave the conveyor belt.

Figure 13 shows the valid data collection interval of PEC differential signals. The positions marked by circles in the figure represent the start and end points of the effective receiving signal range. All four multi-probe arrays detected effective differential signals, and it was determined that the horizontal width of the metal foreign object was 300 mm. By averaging the four differential signals, the effective detection data for the differential signals was from 424.4 ms to 485.4 ms. Based on the initial falling velocity of the metallic foreign object being the same as the operating speed of the belt conveyor (0.3 m/s), the calculated vertical width of the metallic foreign object is 290 mm. The relative error compared to the actual vertical width of 300 mm is 3.33%, which is less than 5% and meets the field testing requirements. Further analysis of the single-period waveform characteristics in the effective detection interval of the differential signals Uref(t) and Bref(t) confirmed the presence of non-ferromagnetic metal. The average peak value of the extracted signals was 45.8 mV, 1.1 mT, and the corresponding average peak times were 0.1 ms and 0.19 ms. According to Figures 10 and 11, it was confirmed that the dropped metal was a 10 mm thick alloy steel Mn13.

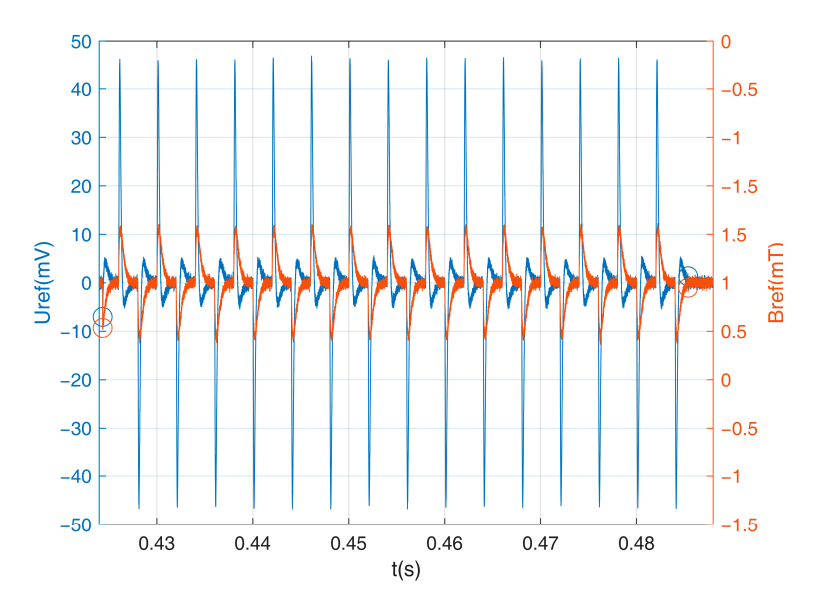


Figure 13. Dual *Y*-axis plot of PEC differential signals and time for the effective detection interval in the field experiment.

5. Conclusions

This study developed a metal foreign object detection system for coal mine crushers. A truncated region eddy current field model was established for the rectangular cross-section coaxial excitation, receiving coils, and Hall sensors interacting with the feeding metal foreign objects. The time-domain expressions for the reflected field induced voltage and magnetic induction intensity were calculated under actual square wave current signals.

Simulation and experimental results demonstrate a close relationship between the effective range, peak value, and peak time of the receiving voltage and magnetic induction signals and the typical characteristics of the metal foreign objects. These characteristics can be used to classify and identify the dimensions, thickness, electrical conductivity, and magnetic permeability of the feeding metal foreign objects. The results of field drop experiments reveal that the horizontal width, thickness, and material of the metal foreign objects were detected with high accuracy. The relative error in detecting the vertical width was less than 5%, which meets the requirements for field detection. This can enhance the recognition rate of metal foreign objects, reduce false alarm rates, and ensure the safe, continuous operation of coal mines.

The signal conditioning module used in this study may be insufficient to handle the strong electromagnetic radiation environment of coal mines. Future research will elaborate on signal preprocessing algorithms tailored to the metallic foreign object detection environment. The research work and findings presented in this paper hold significance for the advancement of classification and recognition methods for feeding metallic foreign objects in crushing operations within coal mines and the development of moving metal detection systems.

Author Contributions: Conceptualization, B.M. and S.Z.; methodology, B.M.; software, B.M.; validation, B.M., Z.Z. and J.M.; formal analysis, B.M.; investigation, B.M.; resources, B.M.; data curation, B.M.; writing—original draft preparation, B.M.; writing—review and editing, Z.Z. and J.M.; visualization, B.M.; supervision, S.Z. All authors have read and agreed to the published version of the manuscript.

Funding: This research received no external funding.

Institutional Review Board Statement: Not applicable.

Informed Consent Statement: Not applicable.

Data Availability Statement: Data are contained within the article.

Conflicts of Interest: The authors declare no conflicts of interest.

References

 Bi, Y.; Pan, Y.; Li, G. A Mixed-feed Identification Method for Sizer Crusher Based on Squeeze-and-excitation Residual Network. IEEE Sens. J. 2024, 24, 21706–21718. [CrossRef]

- 2. Bi, Y.; Pan, Y.; Yu, C.; Wang, M.; Cui, T. An end-to-end harmful object identification method for sizer crusher based on time series classification and deep learning. *Eng. Appl. Artif. Intell.* **2023**, *120*, 105883. [CrossRef]
- 3. Sophian, A.; Tian, G.; Fan, M. Pulsed eddy current non-destructive testing and evaluation: A review. *Chin. J. Mech. Eng.* **2017**, *30*, 500–514. [CrossRef]
- 4. Yan, B.; Li, Y.; Liu, Z.; Ren, S.; Chen, Z.; Lü, X.; Abidin, I.M.Z. Pulse-modulation eddy current imaging for 3D profile reconstruction of subsurface corrosion in metallic structures of aviation. *IEEE Sens. J.* **2021**, *21*, 28087–28096. [CrossRef]
- 5. Gong, Y.; Huang, X.; Liu, Z.; Deng, F.; Wu, Y.; He, C. Development of a cone-shaped pulsed eddy current sensor. *IEEE Sens. J.* **2022**, 22, 3129–3136. [CrossRef]
- 6. Han, Y.; Tao, Y.C.; Shao, C.B.; Yan, H.; Peng, Z.Z. Pulsed eddy currents in ferromagnetic pipes with cladding in nuclear power plants. *Energy Rep.* **2022**, *8*, 104–111. [CrossRef]
- 7. de Haan, V.O.; de Jong, P.A. Analytical expressions for transient induction voltage in a receiving coil due to a coaxial transmitting coil over a conducting plate. *IEEE Trans. Magn.* **2004**, *40*, *371*–*378*. [CrossRef]
- 8. Qian, M.; Wang, Z.; Zhao, J.; Xiang, Z.; Wei, P.; Zhang, J. Identification and classification of bearing steel bars based on low-frequency eddy current detection method. *Measurement* 2023, 213, 112724. [CrossRef]
- 9. Skarlatos, A.; Theodoulidis, T. A modal approach for the solution of the non-linear induction problem in ferromagnetic media. *IEEE Trans. Magn.* **2015**, *52*, 7000211. [CrossRef]
- 10. de Haan, V.O.; Scottini, R. Absolute Wall Thickness Measurement of Conducting Plates Using Pulsed Eddy Currents. *J. Electromagn. Anal. Appl.* **2024**, *16*, 25–41. [CrossRef]
- 11. Theodoulidis, T.; Kriezis, E. Series expansions in eddy current nondestructive evaluation models. *J. Mater. Process. Technol.* **2005**, 161, 343–347. [CrossRef]
- 12. Dodd, C.V.; Deeds, W.E. Analytical solutions to eddy-current probe-coil problems. J. Appl. Phys. 1968, 39, 2829–2838. [CrossRef]
- Li, Y.; Theodoulidis, T.; Tian, G.Y. Magnetic field-based eddy-current modeling for multilayered specimens. *IEEE Trans. Magn.* 2007, 43, 4010–4015. [CrossRef]
- 14. Li, Y.; Tian, G.Y.; Simm, A. Fast analytical modelling for pulsed eddy current evaluation. NDT E Int. 2008, 41, 477–483. [CrossRef]
- 15. Tian, G.Y.; Sophian, A. Reduction of lift-off effects for pulsed eddy current NDT. NDT E Int. 2005, 38, 319–324. [CrossRef]
- 16. Skarlatos, A.; Theodoulidis, T.; Poulakis, N. A fast and robust semi-analytical approach for the calculation of coil transient eddy-current response above planar specimens. *IEEE Trans. Magn.* **2022**, *58*, 6301609. [CrossRef]
- 17. Theodoulidis, T.; Skarlatos, A.; Tytko, G. Computation of eigenvalues and eigenfunctions in the solution of eddy current problems. *Sensors* **2023**, 23, 3055. [CrossRef] [PubMed]
- 18. Huang, R.; Lu, M.; Zhang, Z.; Zhao, Q.; Xie, Y.; Tao, Y.; Yin, W. Measurement of the radius of metallic plates based on a novel finite region eigenfunction expansion (FREE) method. *IEEE Sens. J.* **2020**, 20, 15099–15106. [CrossRef]
- 19. Wen, D.; Fan, M.; Cao, B.; Ye, B.; Tian, G. Extraction of LOI features from spectral pulsed eddy current signals for evaluation of ferromagnetic samples. *IEEE Sens. J.* **2018**, *19*, 189–195. [CrossRef]
- 20. Xue, Z.; Fan, M.; Cao, B.; Wen, D. Enhancement of thickness measurement in eddy current testing using a log–log method. *J. Nondestruct. Eval.* **2021**, 40, 40. [CrossRef]
- 21. Ma, H.; Zhang, Z.; Yin, W.; Li, Y.; Zhou, G. A Rapid Alloy Classification Method Based on Single-Frequency Eddy Current Sensing. *IEEE Trans. Instrum. Meas.* **2024**, *73*, 1–12. [CrossRef]
- 22. Qian, M.; Zhao, J.; Yu, X.; Xiang, Z.; Yu, P.; Wang, F.; Zhang, J. Steel grades classification and heating defects detection of bearing steel bars via pulse eddy current testing. *Phys. Scr.* **2024**, *99*, 106005. [CrossRef]
- 23. Cao, B.; Zhang, Z.; Yin, W.; Wang, D.; Zhang, Z. A Metal Classification System Based on Eddy Current Testing and Deep Learning. *IEEE Sens. J.* 2023, 24, 3266–3276. [CrossRef]
- 24. Huang, P.; Li, Z.; Long, J.; Xu, L.; Xie, Y. Measurement of lift-off distance and thickness of nonmagnetic metallic plate using pulsed eddy current testing. *IEEE Trans. Instrum. Meas.* **2023**, 72, 6006810. [CrossRef]
- 25. Solin, A.; Kok, M.; Wahlström, N.; Schön, T.B.; Särkkä, S. Modeling and interpolation of the ambient magnetic field by Gaussian processes. *IEEE Trans. Robot.* **2018**, *34*, 1112–1127. [CrossRef]
- 26. Tsitsas, N.L. Efficient integral equation modeling of scattering by a gradient dielectric metasurface. *EPJ Appl. Metamaterials* **2017**, 4, 3. [CrossRef]
- 27. Jackson, J.D. Classical Electrodynamics; John Wiley & Sons: Hoboken, NJ, USA, 2021.
- 28. Brown, J.W.; Churchill, R.V. Complex Variables and Applications; McGraw-Hill: New York, NY, USA, 2009.
- 29. Lathi, B.P.; Green, R.A. Linear Systems and Signals; Oxford University Press: New York, NY, USA, 2005; Volume 2.

30. Abramowitz, M.; Stegun, I.A. *Handbook of Mathematical Functions with Formulas, Graphs, and Mathematical Tables*; U.S. Government Print: Washington, DC, USA, 2006.

31. Harrison, D.J.; Jones, L.D.; Burke, S.K. Benchmark problems for defect size and shape determination in eddy-current nondestructive evaluation. *J. Nondestruct. Eval.* **1996**, *15*, 21–34. [CrossRef]

Disclaimer/Publisher's Note: The statements, opinions and data contained in all publications are solely those of the individual author(s) and contributor(s) and not of MDPI and/or the editor(s). MDPI and/or the editor(s) disclaim responsibility for any injury to people or property resulting from any ideas, methods, instructions or products referred to in the content.